Optimized Design of High Power Factor Fault-Tolerant Permanent Magnet Vernier Rim-Driven Machine

Kun Zang, Yaqian Cai, Jingwei Zhu*, Haibo Liao, Mingxuan Li, and Qing Liu

College of Marine Electrical Engineering, Dalian Maritime University, China

ABSTRACT: Fault Tolerant Permanent Magnet Vernier Rim-Driven Machines (FTPMV-RDMs) have attracted much attention due to the advantages of high torque density and good fault tolerant capability. However, the traditional FTPMV-RDMs have a lower power factor which limits their broad application in marine electric propulsion system. This paper proposes a high power factor FTPMV-RDM topology in which the flux-concentrating Halbach array magnets are mounted on a rotor, and isolation slots are arranged on the stator teeth. A preliminary design of the FTPMV-RDM is presented. To tackle the problems of large computational burden and poor accuracy in traditional multi-objective genetic optimization algorithms, a novel optimization design method combining sensitivity-based optimization with sensitivity analysis is proposed. The performance of the machine is analyzed using Finite Element Analysis (FEA), and the results show that the proposed machine topology features a high power factor, high torque density, and strong fault-tolerant capability.

1. INTRODUCTION

In the context of global 'carbon peaking and carbon neutrality', the electrification of ship propulsion has become the mainstream trend in the development of ship dynamical systems. As the core device of ship propulsion electrification, a Rim-Driven Machine (RDM) integrates the machine and propeller into one unit, with the advantages of low vibration and noise, and high efficiency [1, 2].

Currently, the built-in machine of RDM mainly includes brushless direct current machine and permanent magnet (PM) synchronous machine. The torque density of traditional permanent magnet synchronous machine (PMSM) has reached a bottleneck [3, 4]. Moreover, multi-pole multi-slot structure increases the machining difficulty and cost of PMSM [5]. Additionally, RDM operates submerged underwater for extended periods, which makes it susceptible to various electrical faults. In order to ensure the reliability of ship propulsion system, it is necessary that the machine has the capability of fault-tolerance.

PM Vernier machine (PMVM) features high power density, making it particularly suitable for low-speed, high-torque propulsion in marine applications [6]. Ref. [7] introduces a fault-tolerant permanent magnet vernier machine into the built-in machine of RDM, proposing the FTPMV-RDM topology.

FTPMV-RDM combines the merits of PMVM, fault-tolerant machine (FTM), and RDM, possessing advantages such as high torque density, strong fault tolerance, and high efficiency. Essentially, FTPMV-RDM still belongs to the category of PMVM, with one of the reasons hindering its widespread application being the low power factor [8]. On one hand, the low power factor leads to increased inverter capacity and control costs; on the other hand, it weakens the machine's ability to operate under overload conditions. Considering the relatively

large slot opening of the stator in FTPMV-RDM, from the excitation field perspective, the low power factor can be qualitatively interpreted as a larger leakage flux [9]. Ref. [10] conducted a study on the power factor mechanism from the perspective of armature field, indicating that another reason for the low power factor of PMVM is the small proportion of armature working harmonic compared to the total armature flux linkage.

Presently, most methods for improving the power factor of PMVM often come at the cost of sacrificing torque and reducing fault tolerance capacity [11–17], failing to simultaneously meet the requirements of high torque density, high power factor, and strong fault tolerance capacity [18, 19]. In this paper, a novel Halbach array flux-concentrating fault tolerant PM vernier rim-driven machine topology is proposed. To enhance machine performance, a novel sensitivity optimization is employed for its design. The optimized machine features high torque density, high power factor, and strong fault tolerance capacity.

2. MECHANISM ANALYSIS AND STRUCTURE OF MACHINE

2.1. Mechanism Analysis of Power Factor

The power factor is the ratio of the active power P of the machine to the apparent power S, and under the control of $I_d = 0$, ignoring the winding resistance, it can be expressed as:

$$PF = \cos\theta = \frac{P}{S} = \frac{1}{\sqrt{1 + \left(\frac{L_s I}{\psi_m}\right)^2}}$$

$$= \frac{1}{\sqrt{1 + \left(\frac{\omega_r(\psi_{wa} + \psi_{na} + \psi_\delta)}{\omega_r \psi_m}\right)^2}} \quad (1)$$

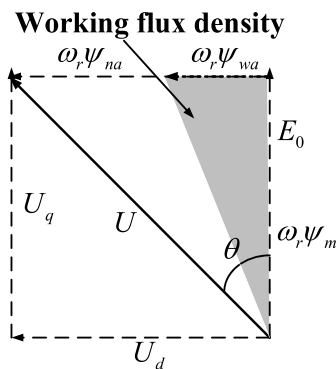* Corresponding author: Jingwei Zhu (zjwdl@dlmu.edu.cn).

Working flux density

FIGURE 1. Phasor diagram of the FTPMV-RDM.

where ψ_m, ψ_{wa}, ψ_{na}, ψ_f, and ψ_δ are PM flux linkage, armature working harmonics flux linkage, armature no-working harmonics flux linkage, and slot leakage flux; L_s is self-inductance; ω_r is current frequency; I is the amplitude of the current; and θ is the angle of the voltage lead current. The phasor diagram of FTPMV-RDM is shown in Fig. 1.

The shaded area in Fig. 1 represents the torque-producing area, which is determined by ψ_m and ψ_{wa}. The larger the shaded area is, the larger torque the machine has [20, 21]. When the armature flux linkage amplitude is fixed, increasing the amplitude of the ψ_m can simultaneously enhance torque and power factor. Furthermore, it can be observed from Fig. 1 that ψ_{wa} only occupies a part of the armature flux linkage, while ψ_{na} is independent of the shaded area and does not participate in the electromagnetic energy conversion, instead, it is related to the magnitude of θ, with higher power factor decreasing. Therefore, the low amplitude of ψ_m and the low proportion of ψ_{wa} to the armature flux linkage can both lead to a decrease in power factor of FTPMV-RDM.

In a word, maintaining ψ_m at a high level, reducing ψ_{na}, and increasing ψ_{wa} can effectively improve the power factor of the machine while ensuring that the torque remains at a high level.

2.2. Machine Topology

The Halbach array flux-concentrating fault tolerant PM vernier rim-driven machine (HFCFTPMV-RDM) proposed in this article is shown in Fig. 2(c), and its PMs structure is shown in Fig. 2(b). To highlight the advantages of the flux-concentrating Halbach structure, reference can be made to the conventional Halbach array fault tolerant PM vernier rim-driven machine (HFTPMV-RDM), whose PMs structure is shown in Fig. 2(a). For comparative purposes, both machines utilize the same hybrid stator structure. The split teeth and straight teeth are arranged alternately, with each split tooth branching into two modulation teeth at the end. Each straight tooth can be considered as a modulation tooth. Both act as magnetic field modulation modules to modulate the air gap magnetic field. Isolation slots are carved on the straight teeth to introduce magnetic barriers, enabling stator modularization. The stator adopts a six-phase single-layer fractional slot concentrated winding, with two sets of six-phase windings. The first set is wound in the forward direction, while the second set is wound in the reverse

direction. The two sets of windings are arranged in a YY offset of $30°$.

The flux-concentrating Halbach structure, based on the Halbach array maintains the air gap length and thickness of the PMs unchanged. An iron core is placed above the radially magnetized PMs, and non-magnetic material is placed below the tangentially magnetized PMs. This structure effectively reduces inter-pole coupling of the PMs and increases the fundamental amplitude of the air gap flux density.

For the proposed HFCFTPMV-RDM, the relationships between armature winding pole-pair P_a and PM pole-pair P_r can be given as:

$$P_a = |iP_r \pm jN_f|, \quad i = 1, 3, 5..., j = 0, 1, 2... \quad (2)$$

where N_f is the number of periods of the stator permeance, and it is closely related to the number of modulation teeth. Especially, the pole ratio of HFCFTPMV-RDM has been introduced, which can be given as:

$$G_{rs} = \frac{P_r}{P_a} \quad (3)$$

Within a certain range, the larger the G_{rs} is, the larger the torque of the machine is, the smaller the power factor is [18], and the fault tolerance capacity will also be affected. Therefore, choosing the appropriate pole ratio to obtain the higher torque density and power factor is an important link in the design of machines.

3. DESIGN OF HFCFTPMV-RDM

3.1. Possible Slot Pole Combinations

HFCFTPMV-RDM adopts six-phase winding, and the number of slots $2N$ can be determined as follows:

$$\frac{2N}{GCD(2N, P_a)} = 6k, \quad k = 1, 2, 3... \quad (4)$$

The $2N$ value of HFCFTPMV-RDM should not be too large. Due to the hybrid stator structure, the number of modulation teeth is as follows:

$$N_s = \frac{3}{2} \times 2N \quad (5)$$

where N_s is the number of modulation teeth. Excessive $2N$ increase N_s, requiring a larger P_r to satisfy Equation (2), which in turn increases G_{rs} and reduces the power factor of the machine. Therefore, slot pole combinations with $2N$ values greater than 36 should not be considered in practical applications. Based on

TABLE 1. Feasible slot-pole combinations.

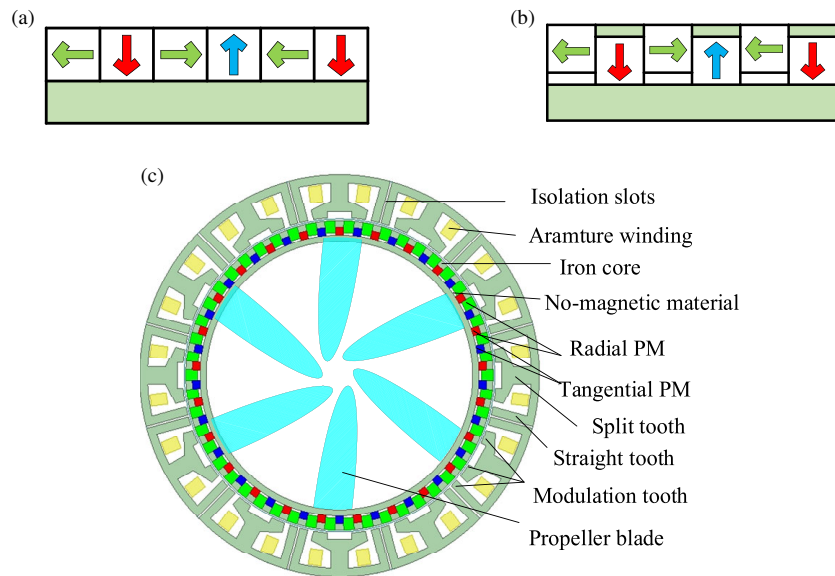| $2N$	P_a	N_s	P_r	G_{rs}
12	5, 7	18	13, 11	2.6, 1.6
24	7, 10, 11, 13	36	29, 26, 25, 23	4.1, 2.6, 2.3, 1.8
36	15, 21	54	39, 33	2.6, 1.6

FIGURE 2. Machine topology. (a) Halbach array. (b) Flux-concentrating Halbach array. (c) HFCFTPMV-RDM.

TABLE 2. Machine performance.

$2N/P_r$	12/11	12/13	24/23	24/25	24/29
THD/%	38.3	41.2	5.21	3.26	4.04
Torque/Nm	24.781	32.617	23.907	32.690	26.352
Ripple/%	15.961	4.179	6.681	1.125	0.159
Power factor	0.6756	0.6679	0.7170	0.7593	0.6941
Coupling coefficient/%	7.20	7.21	1.08	1.06	1.02

the above analysis, feasible slot pole combinations are shown in Table 1.

The coupling coefficient is defined as the ratio of the maximum effective value of mutual inductance to the effective value of L_s. The smaller the coupling coefficient is, the better the fault tolerance capacity is [22]. To ensure fairness, the parameters of machines and the distribution of modulation teeth are the same. Six models with different slot pole combinations were established for simulation analysis, and the results are shown in Table 2.

The machine with N of 12 exhibits significant torque ripple and differences in sinusoidal amplitude of the no load back electromotive force (EMF) due to the decrease in N. On the other hand, the machine with N of 24 has a lower coupling coefficient and higher sinusoidal amplitude of no load back EMF resulting in better performance than the machine with N of 12. Therefore, the machine with slot pole combination of 24/25 is taken as an example for research.

3.2. Parameter Analysis

3.2.1. Modulation Teeth Distribution

The stator structure is depicted in Fig. 3. With one split tooth and one straight tooth spanning a circumferential span as a cycle, the permeance distribution of air gap is illustrated in Fig. 4.

It can be observed that the distribution of modulation teeth significantly influences the air gap permeance, thereby affecting the types and quantities of harmonics in the air gap. When the modulation teeth are evenly distributed, the pole pitch angle θ_s, split tooth angle θ_β, and straight tooth angle θ_α satisfy:

$$\theta_s = \theta_\alpha = \theta_\beta = \frac{2\pi}{N_s} \tag{6}$$

When the modulation teeth are unevenly distributed, these three angles are no longer equal. Define the straight tooth ratio D and split tooth ratio S to represent the degree of uneven distribution of modulation teeth, as shown in (6):

$$D = \frac{\theta_\alpha}{\theta_s}, \quad S = \frac{\theta_\beta}{\theta_s} \tag{7}$$

When the modulation teeth are evenly distributed, $D = S = 1$. If the modulation teeth are unevenly distributed, the values of D and S are no longer equal. Studying the impact of different D and S on the magnetic field modulation effect using performance indicators such as torque and power factor, the simulation results are shown in Fig. 5.

It can be observed that as S increases, the torque and no-load back EMF of the machine initially increase and then decrease, and the optimal S_T value maximizes the torque and no-load back EMF; the effective value of L_s gradually increases.
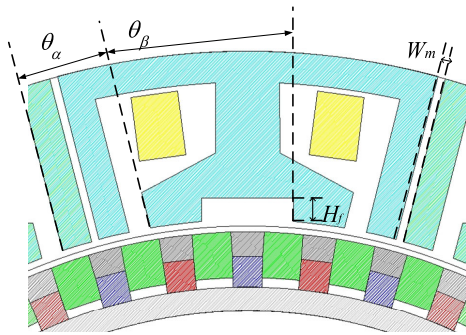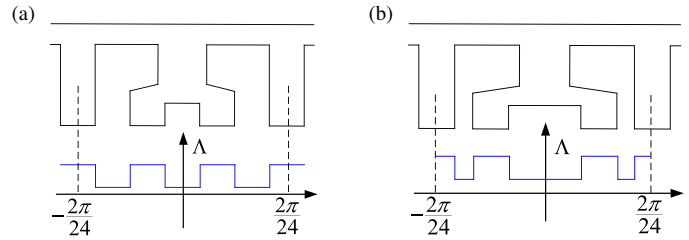
FIGURE 3. Machine stator structure.

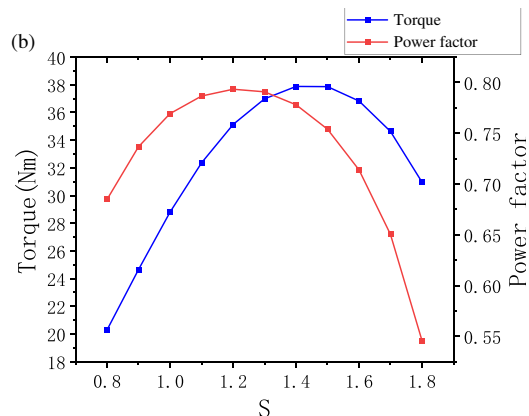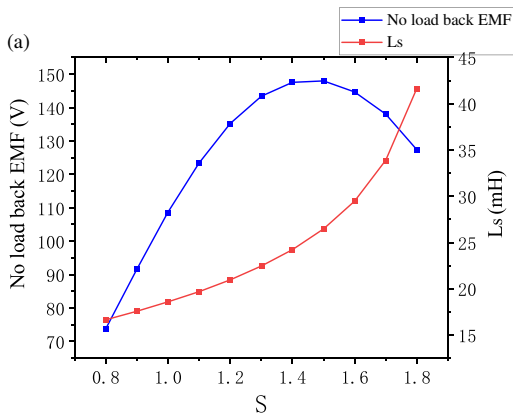FIGURE 4. Permeance expansion diagram. (a) Evenly distributed. (b) Uneven distributed.

FIGURE 5. Effect of S on machine performance. (a) Effect of S on no-load EMF and L_s. (b) Effect of S on torque and power factor.
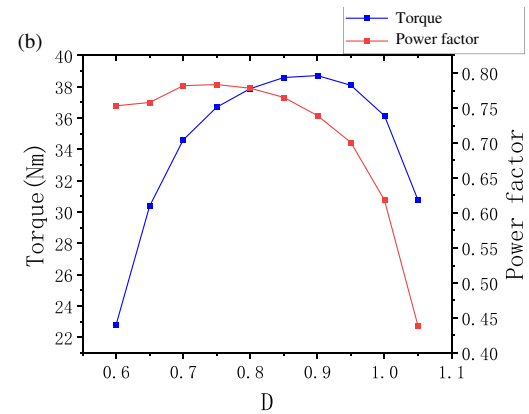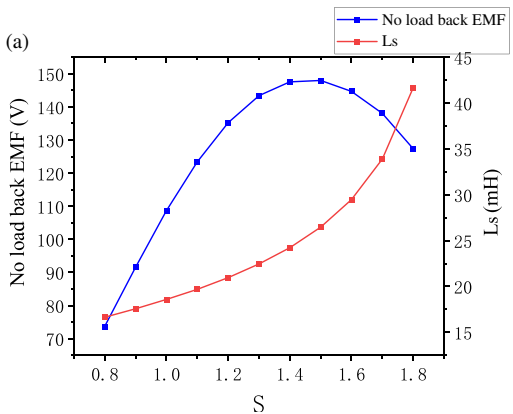

FIGURE 6. Effect of D on machine performance. (a) Effect of D on no-load EMF and L_s. (b) Effect of D on torque and power factor.

The power factor of the machine initially increases and then decreases, with an optimal S_P value maximizing the power factor of machine, but S_P is not equal to S_T.

When $S = S_P$, the torque is 35.14 Nm, and the power factor is 0.82. When $S = S_T$, the torque obtained is 37.88 Nm, and the power factor is 0.80. Compared with the power factor, the difference between the two machines in torque is larger, so S_T, which makes the machine torque maximum, is selected for the next research and discussion.

In the study of D, S is kept at 1.4 for simulation analysis, and the results are shown in Fig. 6. It can be seen that with the increase of D, the torque and no-load back EMF of the machine first increase and then decrease, and the optimal D_T makes the

torque and no-load back EMF maximum. The effective value of L_s increases gradually. The value of the power factor increases first and then decreases. There is an optimal D_P which makes the power factor maximum, but the value of D_P is not equal to D_T.

3.2.2. Effect of Isolation Slots

The armature flux distributions of the machine before and after introducing isolation slots are illustrated in Fig. 7. It can be observed that after introducing the isolation slots, the magnetic circuits of armature no-working harmonics are interrupted. The proportion of working harmonics in the armature flux linkage is
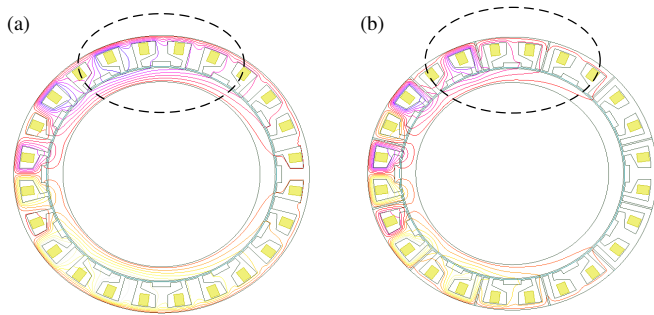
FIGURE 7. Distribution of armature flux. (a) Without isolation slots. (b) With isolation slots.
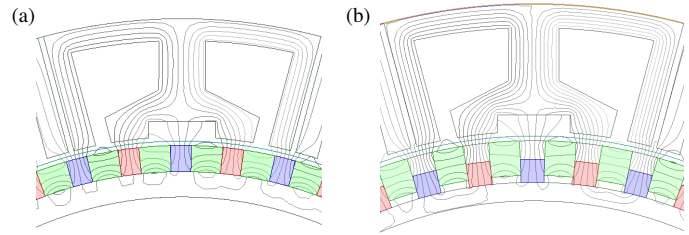

FIGURE 8. Distribution of PM flux. (a) HFTPMV-RDM. (b) HFCFTPMV-RDM.

TABLE 3. Structure parameters of HFCFTPMV-RDM.

Items	Values	Items	Values
Phase number	6	S	1.4
Stator slots	24	D	0.8
PM pole pairs	25	modulation teeth number	36
Stator outer diameter/mm	255	Split tooth width/mm	8
Stator inner diameter/mm	200	Split tooth height/mm	4
Rotor outer diameter/mm	196	Straight tooth width/mm	8.7
Rotor inner diameter/mm	170	Isolation slot width/mm	1.2
Air gap length/mm	2	PM thickness/mm	6

increased. Therefore, implementing isolation slots in the stator modularization can improve the power factor.

3.2.3. Effect of Flux-concentrating Structure

The PM flux distribution comparison between Halbach array and flux-concentrating Halbach array structure is shown in Fig. 8. It can be observed that the flux-concentrating Halbach array reduces the coupling of flux in the PMs, resulting in stronger magnetic focusing. Therefore, it effectively enhances the performance of machine. FEA reveals that the average torque of HFTPMV-RDM is 26.95 Nm with a power factor of 0.71, while that of HFCFTPMV-RDM is 37.88 Nm with a power factor of 0.77.

4. OPTIMIZATION DESIGN

4.1. Novel Optimization Design Method

The structure parameters of HFCFTPMV-RDM are shown in Table 3.

Considering the requirements for electromagnetic performance and fault tolerance capability, the optimization variables selected for analysis include the tooth width W_d, modulation tooth height H_f, isolation slot width W_m, magnetic core thickness R_{in}, PMs width W_t, and PMs thickness H_m. The range of optimization variables is presented in Table 4.

Directly selecting machine torque and power factor as optimization objectives may lead to a higher computational loads,

TABLE 4. Range of optimization variables.

Parameter	Value range
W_d/mm	4.5–9
H_f/mm	4–7
W_m/mm	1–2
R_{in}/mm	1.5–4
W_t/mm	4.5–8
H_m/mm	4–9

resulting in the difference in accuracy of calculation results. To avoid such problems, quantities closely related to torque and power factor can be selected as optimization targets to simplify calculations and improve accuracy. These parameters are defined as T-P sensitive quantities. According to Equation (1) and machine torque equation, the amplitude of ψ_m and the effective value of L_s can be chosen as T-P sensitive quantities to replace torque and power factor as optimization objectives.

Furthermore, the machine model is nonlinear and not suitable for single objective optimization algorithms. Currently, response surface methodology is commonly used for multi-objective optimization. This methodology involves collecting data to establish response surfaces and fitting the machine model for multi-objective optimization. With six optimization parameters in this study, employing traditional multi-objective optimization methods would require a large amount of sampled data to fit the machine response surfaces, resulting in exces-
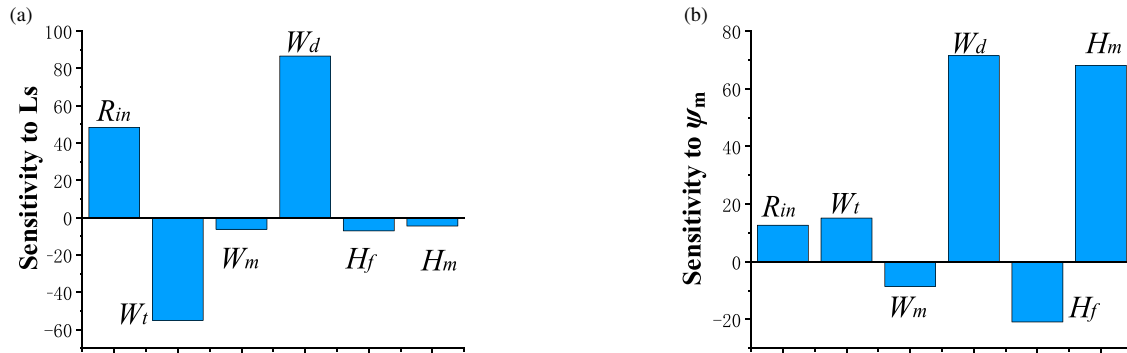
FIGURE 9. The sensitivity of optimization parameters to the optimization objective. (a) The sensitivity of optimization parameters to L_s.. (b) The sensitivity of optimization parameters to ψ_m.
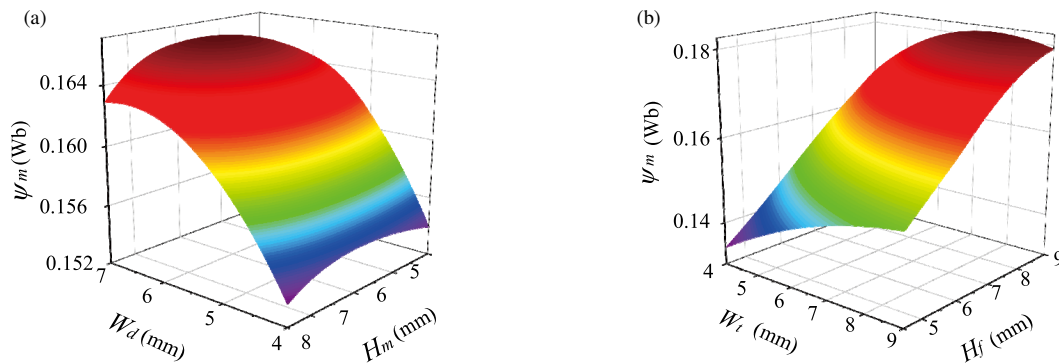

FIGURE 10. Relevant parameters about the response surface of the PM flux linkage. (a) W_d and H_m. (b) W_t and H_f.

sively long optimization times and difficulty ensuring the accuracy of the computational results [23].

This section proposes a novel optimization method that combines sensitivity optimization with sensitivity analysis, reducing computational load while ensuring calculation accuracy. The approach is as follows: Firstly, the design of experiment (DOE) method is applied to obtain quantitative relationships between optimization parameters and objectives, then substituting the experimental results from DOE into the sensitivity Equation (7) to obtain the sensitivity of each optimization parameter to the corresponding objective.

$$S(x) = \frac{N \sum x_i f(x_i) - \sum x_i \sum f(x_i)}{A * B}$$

$$A = \sqrt{N \sum f(x_i)^2 - \left(\sum f(x_i)\right)^2} \qquad (8)$$

$$B = \sqrt{N \sum x_i^2 - \left(\sum x_i\right)^2}$$

where $f(x)$ represents the objective function, and x denotes the optimization parameters. Various sensitivities are illustrated in Fig. 9. Secondly, based on different optimization objectives, the six parameters are ranked by sensitivity, and the top four highly sensitive parameters are selected as the primary optimization parameters for multi-objective optimization. Fine-tuning is then conducted using parameters with lower sensi-

tivities to optimize the two T-P sensitive quantities separately. By this method, the six-dimension multi-objective optimization problem can be simplified into two four-dimension multi-objective optimization problems, thus effectively reducing the computation amount. After optimization, FEA is employed to compute the optimal torque and power factor of machine.

4.2. Implementation of Optimization Process

Taking the optimization of ψ_m as an example, four parameters, W_d, H_m, H_f, and W_t, which are highly sensitive to ψ_m, were selected. A response surface model of the machine is established based on these parameters, as illustrated in Fig. 10.

After obtaining the response surface, multi-objective genetic algorithm is employed to optimize the magnitude of ψ_m. Upon completion of the optimization, the optimal parameter values for achieving the maximum torque are recorded and utilized as initial values for optimizing the L_s effective value. The optimization process for effective value of L_s mirrors that of the ψ_m. The top four parameters with high sensitivity to effective value of L_s, denoted as W_d, W_t, R_{in}, W_m, are selected, and a response surface is established, as shown in Fig. 11. Subsequently, multi-objective genetic algorithm is employed to obtain the optimal solution based on the response surface model.

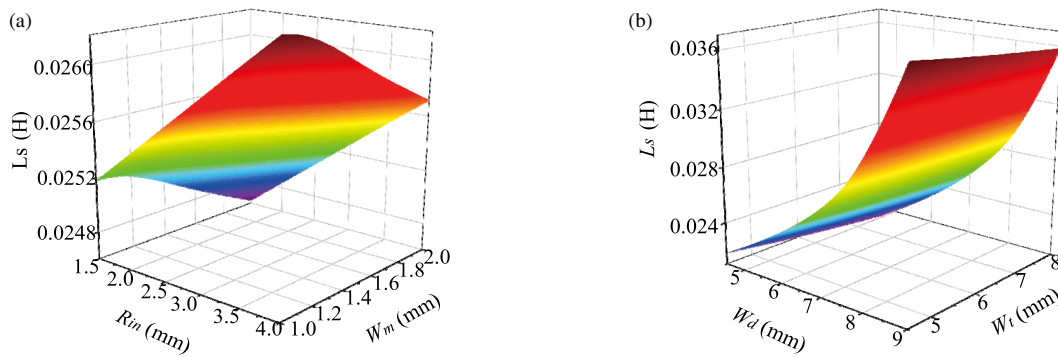Before and after optimization, the parameters are as shown in Table 5.

FIGURE 11. Relevant parameters about the response surface of the L_s. (a) R_{in} and W_m. (b) W_d and W_t.
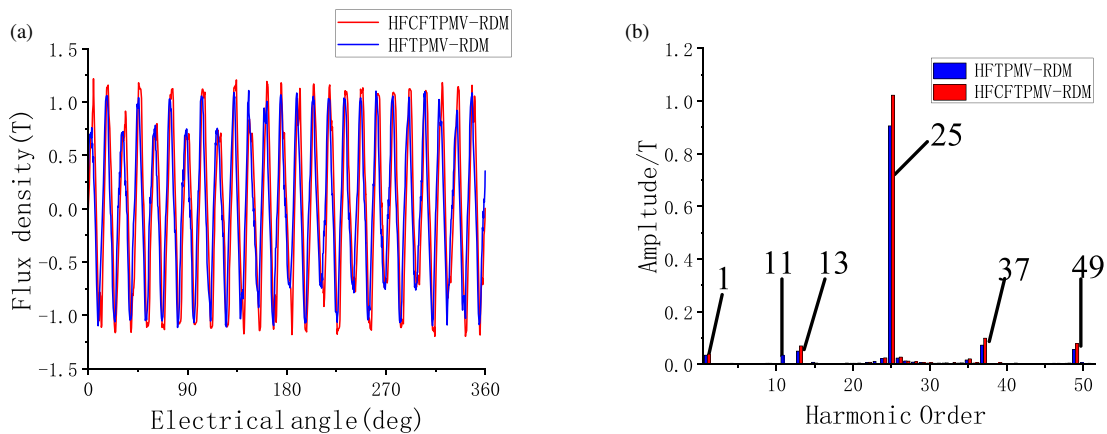

FIGURE 12. No-load air gap magnetic flux density and its Fourier analysis. (a) Flux density. (b) Fourier analysis.

TABLE 5. The machine parameters before and after optimization.

Parameter	Before	After
W_d/mm	5	6.723
H_f/mm	3	4.5
W_m/mm	1.0	1.3
R_{in}/mm	3	4
W_t/mm	5.9	6.6
H_m/mm	6	7.5
Torque/Nm	37.88	41.68
Power factor	0.77	0.81

Calculate the torque and power factor of the machine using the FEA based on the parameters in the table. After optimization, torque is increased by 10.0%, and the power factor is improved by 5.2%. This indicates that sensitivity parameters have an impact on both torque and power factor, thus demonstrating the effectiveness of the proposed optimization method.

5. PERFORMANCE COMPARISON

This section compares the performances of HFTPMV-RDM and HFCFTPMV-RDM. To ensure fairness, both machines have a slot pole combination of 24/25, identical stator structures, and the same amount of PMs material. Both machines were optimized by the proposed optimization method. FEA was used to analyze the air gap flux density, no-load back EMF, torque, and fault-tolerant capability of the two machines.

5.1. Air Gap Flux Density

The air gap flux density and its harmonic analysis for both types of machines are shown in Fig. 12. Fourier analysis reveals that the primary harmonic frequencies for both structures are 25, 1, 11, 13, 37, 49, etc., consistent with the theoretical analysis in Section 2.2. Additionally, due to the magnetizing effect, the fundamental amplitude of HFCFTPMV-RDM is higher.

5.2. No Load Back-EMF

The comparison of no-load back-EMF for both types of machines is illustrated in Fig. 13. It can be observed that the fundamental amplitude of HFCFTPMV-RDM is higher than that of HFTPMV-RDM. Additionally, the total harmonic distortion of HFCFTPMV-RDM is 1.2%, lower than the 2.8% of HFTPMV-RDM. This indicates that the no-load back EMF of the proposed machine exhibits higher sinusoidality.

5.3. Electromagnetic Performance

The torque and power factor of both types of machines at a phase current of 2.8 A are shown in Table 6. With the adoption of the flux-concentrating Halbach array and under the same amount of PMs material, the torque of the machine is increased by 40.9%, and the power factor is improved by 9.5%.
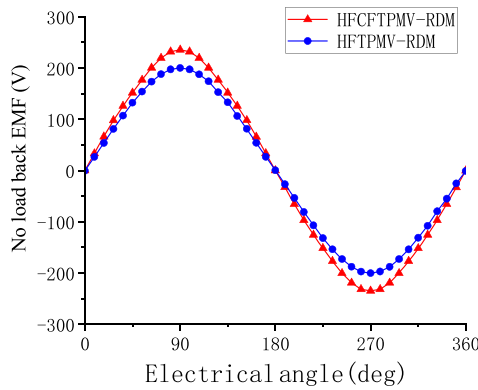
FIGURE 13. Comparison of no-load back EMF.

TABLE 6. Torque and power factor of two kinds of machines.

Items	Torque (Nm)	PF
HFTPMV-RDM	29.58	0.74
HFCFTPMV-RDM	41.68	0.81

5.4. Fault Tolerant Capability

Taking phase A as an example, the effective values of L_s and mutual inductance for both types of machines are presented in Table 7. Since phase A is adjacent to phases U and V in physical space, its mutual inductance has the highest effective value, with coupling coefficients of 3.61% and 3.78%, respectively. The coupling coefficient of the proposed machine is slightly higher than that of HFTPMV-RDM, but its L_s has a larger effective value, indicating stronger suppression of short-circuit currents and maintaining good fault-tolerant capability.

TABLE 7. Self-inductance and mutual inductance of two type of machines.

Items	HFTPMV-RDM	HFCFTPMV-RDM
L_{AA}/mH	25.1212	26.3634
L_{AB}/mH	0.3949	0.4046
L_{AC}/mH	0.3949	0.4046
L_{AU}/mH	0.9082	0.9977
L_{AV}/mH	0.9082	0.9977
L_{AW}/mH	0.0022	0.0162

6. CONCLUSION

A high power factor Halbach array flux-concentrated PM fault-tolerant rim-driven machine topology is proposed in this paper, and its feasibility is verified through simulation results. A novel optimization method combining sensitivity-based optimization with sensitivity ranking is proposed to address the issues of high computational complexity and low accuracy in traditional optimization algorithms. By comparing the performance of HFTPMV-RDM and HFCFTPMV-RDM under the optimal structure, it is demonstrated that the proposed machine exhibits higher torque, larger power factor, and superior fault-tolerant capability.

REFERENCES

[1] Tan, W. Z., X. P. Yan, Z. L. Liu, C. Zhang, Q. Huang, and Z. Tian, "Technology development and prospect of shaftless rim-driven propulsion system," *Journal of Wuhan University of Technology (Transportation Science & Engineering)*, Vol. 39, No. 3, 601–605, 2015.

[2] Guangzhou Haigong, "Successful research and development of shaftless annular thruster," *Guangdong Shipbuilding*, Vol. 39, No. 1, 17, 2020.

[3] Xu, S., Y. F. Huang, P. F. Ma, *et al.*, "Key parameter design and operation characteristic research of rim-driven marine current generators," *Proceedings of the CSEE*, Vol. 39, No. 8, 2449–2459, 2019.

[4] Hu, J. X., J. Y. Wu, and W. P. Chen, "Research of shaftless rim-driven propeller," *Digital Ocean & Underwater Warfare*, Vol. 3, No. 3, 185–191, 2020.

[5] Wang, D., S. B. Jin, Y. S. Wei, P. F. Hu, X. Q. Yi, and J. L. Liu, "Review on the integrated electric propulsion system configuration and its applications," in *Proceedings of the CSEE*, Vol. 40, No. 11, 3654–3662, 2020.

[6] Lin, H., Y. Zhang, H. Yang, S. Fang, and Y. Huang, "Overview and recent developments of permanent magnet vernier machines," in *Proceedings of the CSEE*, Vol. 36, No. 18, 5021–5034, 2016.

[7] Qiao, T., J. Zhu, and R. Ma, "Design and optimization of flux-modulated fault tolerant permanent magnet rim-driven machine," *Journal of Dalian Maritime University*, Vol. 47, No. 4, 100–107, 2021.

[8] Qiao, T., J. Zhu, and X. Wang, "Design and optimization of a flux-modulated fault-tolerant permanent magnet rim-driven machine with combined stator to improve torque density," *IEEE Transactions on Energy Conversion*, Vol. 38, No. 1, 75–88, Mar. 2023.

[9] Zhao, Y., D. Li, X. Ren, and R. Qu, "Investigation of permanent magnet vernier machines from armature field perspective," *IEEE Journal of Emerging and Selected Topics in Power Electronics*, Vol. 10, No. 3, 2934–2945, Jun. 2022.

[10] Li, D., R. Qu, and T. A. Lipo, "High-power-factor vernier permanent-magnet machines," *IEEE Transactions on Industry Applications*, Vol. 50, No. 6, 3664–3674, 2014.

[11] Ching, T. W., K. T. Chau, and W. Li, "Power factor improvement of a linear Vernier permanent-magnet machine using auxiliary DC field excitation," *IEEE Transactions on Magnetics*, Vol. 52, No. 7, 1–4, Jul. 2016.

[12] Zhao, X. and S. Niu, "Design and optimization of a new magnetic-geared pole-changing hybrid excitation machine," *IEEE Transactions on Industrial Electronics*, Vol. 64, No. 12, 9943–9952, Dec. 2017.

[13] Rao, J., R. Qu, D. Li, and Y. Gao, "A novel surface permanent magnet vernier machine with Halbach array permanent magnet in stator slot opening," in *2016 IEEE Conference on Electromagnetic Field Computation (CEFC)*, Miami, FL, USA, 2016.

[14] Yang, H., Z.-Q. Zhu, H. Lin, H. Li, and S. Lyu, "Analysis of consequent-pole flux reversal permanent magnet machine with biased flux modulation theory," *IEEE Transactions on Industrial Electronics*, Vol. 67, No. 3, 2107–2121, Mar. 2020.

[15] Du, Z. S. and T. A. Lipo, "Design of an improved dual-stator ferrite magnet vernier machine to replace an industrial rare-earth IPM machine," *IEEE Transactions on Energy Conversion*, Vol. 34, No. 4, 2062–2069, Dec. 2019.

[16] Xu, L., G. Liu, W. Zhao, X. Yang, and R. Cheng, "Hybrid stator design of fault-tolerant permanent-magnet vernier machines for direct-drive applications," *IEEE Transactions on Industrial Electronics*, Vol. 64, No. 1, 179–190, Jan. 2017.

[17] Xu, L., W. Wu, and W. Zhao, "Airgap magnetic field harmonic synergetic optimization approach for power factor improvement of PM vernier machines," *IEEE Transactions on Industrial Electronics*, Vol. 69, No. 12, 12 281–12 291, Dec. 2022.

[18] Ren, X., D. Li, R. Qu, Z. Yu, and Y. Gao, "Investigation of spoke array permanent magnet vernier machine with alternate flux bridges," *IEEE Transactions on Energy Conversion*, Vol. 33, No. 4, 2112–2121, Dec. 2018.

[19] Qiao, T., J. Zhu, and X. Wang, "Performance comparison of spoke array fault tolerant PM vernier rim driven machine with different numbers of flux modulation poles," *Progress In Electromagnetics Research M*, Vol. 105, 55–65, 2021.

[20] Zhao, Y., X. Ren, X. Fan, D. Li, and R. Qu, "A high power factor permanent magnet vernier machine with modular stator and yokeless rotor," *IEEE Transactions on Industrial Electronics*, Vol. 70, No. 7, 7141–7152, Jul. 2023.

[21] Zhao, Y., D. Li, X. Ren, Z. Liang, and R. Qu, "Low pole-pair ratio integration design of permanent magnet vernier machine with improved power factor," *IEEE Transactions on Industrial Electronics*, Vol. 71, No. 3, 2820–2830, Mar. 2024.

[22] Ma, R., J. W. Zhu, and X. H. Xu, "Design and analysis of a fault-tolerant pemanent magnet rim driven machine," *Small & Special Electrical Machines*, Vol. 47, No. 6, 45–48, 2019.

[23] He, W., J. Zhu, Z. Wang, J. Yue, and T. Zhao, "Optimization of flux-concentrating consequent-pole permanent magnet fault tolerant vernier rim-driven motor," *Progress In Electromagnetics Research C*, Vol. 135, 241–253, 2023.